JOURNAL OF GEOPHYSICAL RESEARCH, VOL. ???, XXXX, DOI:10.1029/,

The effects and correction of the geometric factor for the POES/MEPED electron flux instrument using a multi-satellite comparison.

Ian C. Whittaker,[1] Craig J. Rodger,[1] Mark A. Clilverd[2], and Jean-André Sauvaud[3]

Abstract. Measurements from the POES Medium Energy Proton and Electron Detector (MEPED) instrument are widely used in studies into radiation belt dynamics and atmospheric coupling. However, this instrument has been shown to have a complex energy dependent response to incident particle fluxes, with the additional possibility of low-energy protons contaminating the electron fluxes. We test the recent Monte-Carlo theoretical simulation of the instrument by comparing the responses against observations from an independent experimental dataset. Our study examines the reported geometric factors for the MEPED electron flux instrument against the high energy resolution Instrument for Detecting Particles (IDP) on the DEMETER (Detection of Electro-Magnetic Emissions Transmitted from Earthquake Regions) satellite when they are located at similar locations and times, thereby viewing the same quasi-trapped population of electrons. We find that the new Monte-Carlo produced geometric factors accurately describe the response of the POES MEPED instrument. We go on to develop a set of equations such that integral electron fluxes of a higher accuracy are obtained from the existing MEPED observations. These new MEPED integral fluxes correlated very well with those from the IDP instrument (>99.9% confidence level). As part of this study we have also tested a commonly used algorithm for removing proton contamination from MEPED instrument observations. We show that the algorithm is effective, providing confirmation that previous work using this correction method is valid.

1. Introduction

The POES (Polar Orbiting Environmental Satellite) network of polar orbiting satellites (formerly known as TIROS - Television and InfraRed Observation Satellite) is operated by NOAA (National Oceanic and Atmospheric Administration). These satellites have been running from NOAA-05 in 1978 up to the present in Sun-synchronous orbits at varying Equatorial Crossing Times (ECT). EUMETSAT added the MetOp-02 satellite to the POES network with the same particle instrumentation in May 2007. The MEPED (Medium Energy Proton and Electron Detector) instrument is the focus of our study and the data have been widely used in previous research [e.g *Callis*, 1997; *Millan et al.*, 2010; *Carson, Rodger and Clilverd*, 2013]. The MEPED instrument is an electron flux detector, which takes measurements at both 0° and 90° angles from the radial line to the satellite for 3 integral energy ranges. A full description of the instrument is included in Section 2.1. The main advantage of using this instrument for magnetospheric research comes from it's long data duration, which spans more than two solar cycles with almost continuous data coverage. The same instrument is on multiple satellites allowing spatially different measurements to be made at simultaneous times.

[1]Department of Physics, University of Otago, Dunedin, New Zealand.
[2]British Antarctic Survey (NERC), Cambridge, UK.
[3]IRAP, CNRS-University of Toulouse, Toulouse, France.

0148-0227/14/$9.00

The accuracy of the POES/MEPED instruments, as well as the inferred electron spectra, are important when studying radiation belt physics. This is especially true when these datasets are used to compare with space or ground-based experiments, or used to drive a variety of models including chemistry-climate coupled models [*Wissing and Kallenrode*, 2009]. In addition wave-particle interactions which drive acceleration, transport and loss are dependent upon wave-frequency [e.g., *Tsurutani and Lakhina*, 1997], and the electron energy spectra can also provide evidence of these physical processes at work, for a full review see *Thorne* [2010].

In particular, energetic electron precipitation (EEP), which is strongest during geomagnetic storms, is of great interest as the particle energy determines the altitude at which the majority of its energy is deposited [e.g., *Turunen et al.*, 2009, Fig.3]. Electrons with energies ∼100 keV cause peak ionization changes at ∼80 km altitude while ∼1 MeV electron energy peaks at ∼62 km altitude. This has major implications for atmospheric chemistry as precipitating charged particles produce odd nitrogen (NO_x [*Newnham et al.*, 2011]) and odd hydrogen (HO_x [*Verronen et al.*, 2011]) in the Earth's atmosphere. These odd particles can then catalytically destroy ozone due to their longer lifetime at these altitudes [*Solomon, Crutzen and Roble*, 1982; *Brasseur and Solomon*, 2005].

The "basic" approach for converting MEPED counts into fluxes makes use of a simple geometric factor, where the count values are multiplied by 100 $cm^{-2}sr^{-1}$ [*Evans and Greer*, 2004]. Various instrument issues and uncertainties with the MEPED observations have been identified since 2000. One example is radiation damage [*Galand and Evans*, 2000], which affects the proton telescopes more than the electron telescopes due to a metallic foil shield in front of the electron aperture. As our study is looking exclusively at corrections to the electron flux observations, in our case the most important issues concern proton contamination of the electron channels and electron detector efficiency. An approach for proton contamination removal was initially provided by *Lam et al.* [2010, Appendix A] and more recently, modeled calibration values using a Monte-Carlo method have been calculated by *Yando et al.* [2011]. The *Yando et al.* [2011] study used the GEANT 4 code to simulate the geometric factor required to calculate the MEPED charged particle flux. Their analysis showed significant contamination between particle types as well as a variation in detector efficiency with energy (the energy cutoffs were also shown to be continuous rather than discrete). The conclusions of *Yando et al.* [2011] have been further confirmed by *Asikainen and Mursula* [2013] using a variation of the same code on both the SEM-1 and SEM-2 (Space Environmental Monitor) versions of the MEPED instrument.

The SEM-2 version MEPED data corrections performed using methods from *Lam et al.* [2010, Appendix A] have been applied in a large number of studies using the POES satellites [e.g. *Meredith et al.*, 2011; *Turner et al.*, 2012; *Li et al.*, 2013; *Rodger et al.*, 2013]. The method used by *Lam et al.* [2010] involves estimating the proton flux in the relevant contamination energy ranges using a bowtie method [*Selesnick and Blake*, 2000], these are then directly subtracted from the electron fluxes. An updated version of the correction algorithm can be found in *Green* [2013] which mixes the proton flux bowtie method with the *Yando et al.* [2011] proton response functions.

The goal of our study is to examine the corrected data (from *Lam et al.* [2010, Appendix A]) and also to apply corrections from *Yando et al.* [2011] to the uncorrected MEPED data. We investigate the validity of these corrections through comparison with observations made onboard the DEMETER (Detection of Electro-Magnetic Emissions Transmitted from Earthquake Regions) satellite in an effort to determine the difference between the electron flux correction methods.

2. Instrumentation

2.1. MEPED instrument

The NOAA/POES MEPED sensor provides two kinds of particle count rate measurements including two directional measurements of protons (0.03->6.9 MeV, with 6 energy steps labeled P1 to P6) and electrons (0.03-2.5 MeV, in 3 energy steps, labeled E1 (>30 keV), E2 (>100 keV) and E3 (>300 keV)). There are two telescopes for both protons and electrons pointing in different directions, each with a viewing width of $\pm 15^\circ$. The 0° detector is directed along the Earth-spacecraft radial direction, and the axis of the 90° detector is perpendicular to this (anti-parallel to the spacecraft velocity vector). Modeling work has established that the 0° telescope monitors particles in the atmospheric bounce loss cone that will enter the Earth's atmosphere below the satellite when the spacecraft is poleward of L≈1.5-1.6, while the 90° telescope monitors trapped fluxes or those in the drift loss cone, depending primarily upon the L shell [*Rodger et al.*, 2010b, Appendix A].

The MEPED instrument has been updated as part of the SEM-2 subsystem and these changes have been implemented from NOAA-15 to NOAA-19 and the MetOp-2 satellite. *Asikainen and Mursula* [2013] showed that the MEPED instruments on SEM-1 and SEM-2 systems do not have similar geometric factors. For our study we consider only SEM-2, and hence only the satellites listed above are considered, as the geometric factor values given in *Yando et al.* [2011] are for SEM-2 application alone, (The SEM-1 system having previously been compared in a similar way to the CRRES satellite [*Tan, Fung and Shao*, 2007]). A full description of the SEM-2 system which includes the MEPED instrument can be found in *Evans and Greer* [2004].

2.2. IDP instrument

The DEMETER satellite was launched in June 2004, flying at an altitude of 670 km (after 2005) in a Sun-synchronous orbit with an inclination of 98°. The final data was received in March 2011 before the deorbiting of the satellite.

The IDP (Instrument for Detecting Particles) used in our study is an electron spectrometer mounted aboard the DEMETER micro-satellite. The IDP has 256 energy channels which can be operated in burst mode (all channels sampled at 1s) or the more common survey mode (128 channels at 4s resolution with a constant 17.9 keV bin width), with an energy range from 72 keV to 2.3 MeV with the final channel collecting electron fluxes from 2.3 MeV to greater than 10 MeV. The first channel has no lower energy limit (<72-90 keV) and so is also an integral channel rather than a differential channel. As the first and last channels cause problems with spectral fitting and total flux values [*Whittaker et al.*, 2013] these two channels are not used in our study. The detector looks perpendicular to the orbital plane of the satellite, which is almost polar and circular with a viewing angle of $\pm 16^\circ$. The main instrument error at energies less than 800 keV is statistical and has an $\pm 8\%$ energy uncertainty. This corresponds to an average flux uncertainty of less than 10%.

For most locations the IDP observes electrons with pitch angles in the drift loss cone. A full description of the instrument can be found in *Sauvaud et al.* [2006] and a discussion of the pitch angles sampled as well as uncertainties can be found in *Whittaker et al.* [2013].

3. Method

3.1. Geometric factors for MEPED

The Geometric Factor values in *Yando et al.* [2011] are used to turn a flux incident on the POES-telescopes into what the instrument reports as a count rate. In practice, we have the POES-reported count rates, and wish to determine the fluxes from these values. Converting instrument counts into an accurate flux is difficult as there are multiple different ways that a proton and electron flux could result in the values reported by the instrument. This means that the effect of the geometric factors given in *Yando et al.* [2011] on the MEPED instrument spectra need to be tested.

To test the accuracy of the Yando geometric factors and also to determine the accuracy of previous correction algorithms, a proxy for the real electron flux needs to be used. The DEMETER satellite has a similar orbit to the NOAA/MetOp satellites (Sun-synchronous) at a slightly lower altitude (670 km opposed to ∼800 km of the POES satellites) and the mission was active while a large number of the POES satellites were also active. Our justification for assuming DEMETER is a good proxy for the true electron flux comes from its high energy and time resolution as well as its lack of proton contamination. We note that *Sauvaud et al.* [2006] reports that "The optic has also an aluminium foil with a thickness of 6mm to avoid parasitic light and to stop protons with energies lower than 500 keV".

Both DEMETER and the POES satellites have electron-measuring instruments which sample the same pitch angle ranges. Application of the Yando geometric factors to the DEMETER/IDP differential fluxes, which are assumed to be close to the actual fluxes in space, should yield the count rates observed by POES/MEPED once integrated. These simulations of the MEPED counts, when multiplied by 100 $cm^{-2}sr^{-1}$, will provide electron flux values for comparison with the E1, E2 and E3 channels of POES. A pictographic description of this process can be seen in the top line of Figure 1.

Due to the pointing direction of the IDP instrument, only the MEPED 90° detectors can be used in this comparison. The results from *Yando et al.* [2011] and *Asikainen and Mursula* [2013] as well as the instrument description in *Evans and Greer* [2004] do not suggest any major differences in the 0° and 90° telescopes. This means any relation which works for one detector direction should work for both. Our study will also refer to uncorrected flux data from the MEPED instrument, which we define as electron counts multiplied by the (non-energy dependent) geometric factor of 100 $cm^{-2}sr^{-1}$ [*Evans and Greer*, 2004] necessary to produce an integral flux value, making no corrections for either proton contamination or electron detection efficiency.

3.2. Comparison criteria

Flux comparisons are performed when one of the POES satellites is sampling approximately the same flux distribution as the DEMETER satellite (10:00 ECT). This limits the available POES satellites to those in approximately the same local time sector as DEMETER. The appropriate satellites where the orbital paths are close are NOAA-16 (09:00 ECT) and MetOp-2 (09:31 ECT). However, in our study MetOp-2 is used exclusively due to the higher number of positional matches with DEMETER. The matching criteria are based on being at similar L shells and longitudes at approximately the same time. These criteria are discussed in Section 6.1.

Global median electron flux maps were produced which are shown in Figure 2, with a 0.5° resolution. The maps include 4 years worth of data from January 2007 to December 2010 inclusive and show the integral energy range of >100 keV. This energy range was used as it required no extrapolation of data from the IDP instrument to estimate fluxes at energies below 90 keV (see Section 5.1). The top left panel shows the median flux map for the MEPED instrument onboard MetOp-2. The uncorrected flux values are used, and thus are after the 100 $cm^{-2}sr^{-1}$ non energy dependent multiplication applied to the raw counts. The top right panel shows the same time period for the DEMETER IDP instrument with the >100 keV fluxes on a $\log_{10}$ color scale. Due to DEMETER operation limitations, the MetOp-2 data coverage is far more expansive in terms of latitude. The noise floor of the MEPED instrument is clearly seen at a flux of 100 $e.cm^{-2}sr^{-1}s^{-1}$. By comparison with the IDP instrument panel it is clear that this noise floor overestimates the actual flux in some regions by over 2 orders of magnitude. There is also a slight difference in the shape of the South Atlantic Magnetic Anomaly (SAMA), with MEPED picking up an extension of the area around 80°W, 15°S.

To provide a more like-for-like comparison the median integral flux map for IDP is replotted so that the noise floor is limited to the same as the MEPED instrument (10^2 $e.cm^{-2}sr^{-1}s^{-1}$). This new map is displayed in the lower left panel of Figure 2, showing a far more similar image to the top left panel (MEPED median flux map). The lower right panel of Figure 2 shows a ratio of the upper and lower left panels. Using the noise floor altered IDP data forces all the regions of low flux (i.e. low L shell areas) to appear the same. The color scale on this map shows red where the median IDP flux is higher, blue where the median MEPED flux is higher and white where the values are approximately equal. In the outer radiation belt the MEPED instrument sees slightly more flux, which may be due to its higher altitude. The inner radiation belt shows the opposite with IDP seeing marginally higher fluxes. Again this could be an altitude effect with IDP seeing different amounts of the drift and bounce loss cones than MEPED (see the pitch angle distribution maps in *Rodger et al.* [2010a, Figure A2] and *Whittaker et al.* [2013, Figure 2] for MEPED and IDP respectively). The SAMA generally shows much higher fluxes for the IDP instrument, except for the collar north of the SAMA. The differences in global flux are mostly within the ±200% difference range (factor of 3) with only the SAMA producing differences above this.

The small flux difference in the areas outside the SAMA shows that the instruments should be observing similar electron fluxes, with this confirmed we now move onto determining the effect of the Yando geometric factors on the POES data.

4. Proton contamination

The first step to decontaminating the electron fluxes is to remove the effect of the protons which can produce false electron counts in the MEPED observations. As shown by Yando, each MEPED electron channel has a different reaction to energy-varying proton fluxes. The process of removing these can be done on a case by case basis but we have developed an average case study approach for a more efficient removal process. To produce the best proton contamination removal approach all six available POES satellites are used, this not only ensures a higher resolution of flux map but also ensures that the proton detectors on each satellite reacts the same. Figure 3 shows global maps of the MEPED >30 keV proton fluxes and the fitted power-law spectral index for the proton fluxes for the month of January 2012. The power law fit is of the form $j = j_0 E^{\gamma}$ where j is integral proton flux, j_0 is referred to as the amplitude ($p^+.cm^{-2}sr^{-1}s^{-1}.keV^{-1}$) and γ is the spectral index. The >30 keV fluxes are produced by combining all six proton channels. The left panels of Figure 3 show the 0° detector response and the right panels show the 90° results. The top panels show median global flux distributions where the SAMA and outer radiation belts are clearly visible. The middle panels show the median proton power-law spectral index. Here again the SAMA is clearly visible as having a relatively hard spectral index (close to zero) suggesting near constant fluxes irrespective of energy, likely due to the intense high energy protons from the inner proton belt overwhelming the instrument in the SAMA [*Rodger et al.*, 2013]. In contrast, in the areas of interest for radiation belt studies, there are softer spectral indicies (between -2 and -4). The lower panels show scatter plots of the proton fit coefficients. The amplitude and spectral index are very strongly correlated and this is the basis for simplifying the proton decontamination. As a test the same maps in Figure 3 were reproduced for January 2011 (not shown). The maps from both dates looked almost identical and the relationships between fitted amplitude and power law spectral index had a very small variation in coefficient value from the 2012 case.

The power law spectral index maps presented in the middle panels of Figure 3 show that the fitted proton power-law spectral index gradually decrease with distance from the equator. If we combine this with the relation in the lower panels it means there are only a few configurations that the proton flux spectrum can take at any particular point. Sample fits ranging from proton spectral indicies of -0.2 to -10 in 0.2 increments are created and multiplied by the Yando electron instrument response equations to produce the electron contamination flux due to protons expected for each MEPED electron channel and a given proton spectral index. These are plotted in the top panel of Figure 4 which shows a smooth transition with proton spectral index and the contamination on each channel. The lower panels of Figure 3 show that the fitted amplitude to power law spectral index relation has almost identical coefficients for the 0° and 90° telescopes. Considering the 0° and 90° electron detectors are assumed to be the same, these proton contamination removal equations should be the same for both telescope look directions. In cases where the spectral index is less than -2, Figure 4 (top) shows the proton contamination values are low, particularly for the E2 and E3 detectors. Referring back to the central panels of Figure 3 the spectral index is greater than -2 in the equatorial regions, the SAMA, and very high polar geomagnetic latitudes - areas which do not include the radiations belts. These areas are generally removed from studies involving the radiation belts (including this one) due to their low fluxes. The proton contamination equations which can be used to remove typical levels of proton contamination for each MEPED electron detector channel for both telescopes are given below:

$$E1_+ = 2309e^{0.11b_p} + 1.32 \times 10^4 e^{1.92b_p} + 443b_p - 1272 \quad (1)$$

$$E2_+ = 1.32 \times 10^4 e^{1.746b_p} + 175 \quad (2)$$

$$E3_+ = 1.24 \times 10^4 e^{1.936b_p} \quad (3)$$

Where,

$E1_+$: is the E1 channel flux increase due to proton contamination.

b_p : is the proton fit spectral index

The values shown in Figure 3 are averaged over a month and any changes during short-lived events such as geomagnetic storms could be masked. To determine if the relation of the proton power law spectral index to proton contamination fluxes are the same at quiet and storm times, we took the Kp values for 2011 from the SPIDR data service [*SPIDR, NGDC/NOAA*, 2013]. While a common definition of a storm is Kp>4.7 [*Space Weather Prediction Center, NOAA*, 2011], we used the slightly stronger criteria of Kp>5.3. In 2011 there are 20 three hour periods which have a Kp value >5.3 which occur on 9 separate days. The MEPED proton observations from those time periods have been examined in a similar way to that shown in Figure 3. The spectral index to amplitude relation again follows an exponential fit (not shown) with the 90 degree telescope being almost the same as the all-Kp case in Figure 3, while the fitted relationship for the 0-degree telescopes has only small differences in the coefficients. We therefore use the non-storm case, as it is derived from a much larger dataset.

To determine the effect that a geomagnetic storm would have on the proton contamination of POES/MEPED electron channels, we again determine the electron instrument response to these protons. The middle panel of Figure 4 shows the storm-time 0 degree detector proton contamination flux which would be present on the electron channels. For the spectral indicies between 0 and -2 there is significantly less contamination, however, when the spectral index is sharper than -7 the contamination increases. The storm-time contamination effect for the 90 degree detector is midway between the all-Kp case and 0-degree detector. When viewing these panels it is important to note that proton fit spectral indicies are rarely less than -5, the values lower than this have been included out of completeness.

Our analysis of proton contamination in the MEPED electron flux observations (leading to Equations (1)-(3)) demonstrate the quantitative effect of the proton contamination in the radiation belts. From Figure 3 the average spectral index in the radiation belts is approximately -4, giving proton contaminations of 547, 187 and 5 e.cm^{-2}sr^{-1}s^{-1} for each energy channel. From Figure 2, the average >30 keV trapped electron flux in the radiation belts is 5×10^4 e.cm^{-2}sr^{-1}s^{-1} giving a proton contamination of approximately 1%. The >100 keV channel has an average electron trapped flux of 10^4 e.cm^{-2}sr^{-1}s^{-1} giving a proton contamination of 1.8%, while the >300 keV channel which contains lower electron fluxes (300 e.cm^{-2}sr^{-1}s^{-1}) has an average contamination value closer to 2%. This correlates well with the results of *Lam et al.* [2010] who stated that the E3 channel suffered the most from proton contamination, although the effects of the electron detection efficiency on the E3 channel are more likely to be responsible for the conclusion reached by these authors. *Yando et al.* [2011] stated that protons have a 20% "accessibility" to the electron telescopes above 200 keV, from Figure 3 we can see that the fluxes of >200 keV protons will be very small except for spectral indicies close to 0. However, proton contamination will be much more significant during solar proton events or in locations where there are high proton fluxes (i.e. the SAMA, as shown by *Rodger et al.* [2013]). In the SAMA where the proton power law spectral index is closer to 0 the noise floor can be increased by several orders of magnitude, giving an erroneously high value for the electron flux in this region. This is the most likely cause of the flux differences between POES and DEMETER in the SAMA exceeding the ±200% value as described in Section 3.2. At a flux of 100 e.cm^{-2}sr^{-1}s^{-1}, the noise floor of the instrument, the proton contamination at worst increases this flux by an order of magnitude. At higher electron fluxes the proton contamination is a smaller percentage of the flux and hence, becomes less important. We only perform our flux comparisons in these high electron flux areas to avoid any SAMA or SPE contamination errors from affecting the results.

5. Applying the Yando geometric factors

The next step after determining proton contamination is to calculate what effect the detector efficiency has on the electron count measurements. The geometric factors provided by Yando include this electron efficiency factor and we will use the DEMETER data to determine how higher resolution electron flux measurements will be affected and provide a way of reversing this for application to the POES/MEPED instrument. We have shown that the DEMETER satellite observes similar electron fluxes to the POES MetOp-02 satellite using a mutually covered energy range (>100 keV). However, the two satellites measure electron counts in different energy ranges and types (differential and integral) which needs to be accounted for during the following inter-comparisons.

5.1. Converting IDP differential flux to MEPED-like observations

The most important issue with comparing the data from the IDP instrument and the MEPED instrument is the difference in energy resolution. The 126 channels of the IDP instrument provide discrete energy ranges from 90 keV to 2.33 MeV, while the MEPED instrument provides integral flux of >30 keV, >100 keV and >300 keV. Converting an IDP spectrum into integral values is possible by interpolating the data so it spans a given energy range and then integrating with respect to energy. Care has to be taken when recreating MEPED data from IDP observations as the lowest energy value of the IDP instrument that we use is 90 keV. Thus a large scale interpolation (equivalent to the width of 3.5 IDP energy channels) is required to estimate the flux at an energy value of 30 keV, the lowest energy sampled by POES. The importance of this is discussed in Section 6.2.

There is also the issue of erroneous high energy electron flux data from the IDP instrument. This is the result of two lower energy particles hitting the IDP detector at the same time and being mistaken for a single high energy particle (the sampling rate of the IDP instrument is 0.6 MHz). The fluxes of these "false" high energy particles are negligible when it comes to a total flux determination but can affect fitting (and extrapolation to higher energies). This issue is discussed more fully in *Sauvaud et al.* [2006], *Gamble* [2011] and *Whittaker et al.* [2013]. To avoid this a cutoff to the IDP spectrum is applied when the flux drops below 1 e.cm^{-2}sr^{-1}s^{-1}keV^{-1}. All the data from the second channel (90 keV) to the channel where this cutoff value occurs are used and interpolated between 10 keV and 10 MeV (the energy limits of the Yando geometric factor values). To produce IDP integral values, the sum of these interpolated flux values from 30 keV to 10 MeV are used to produce the IDP >30 keV electron flux value, 100 keV to 10 MeV for the IDP >100 keV value and 300 keV to 10 MeV for the IDP >300 keV flux. Note that the Yando geometric factors indicate that the MEPED detectors are weakly sensitive to electrons with energies below the strict energy cutoffs implied by the named range, such that some fluxes in the energy range 10-30 keV will be detected by the >30 keV integral channel. To produce integral values which simulate the MEPED data, the interpolated fluxes from 10 keV to 10 MeV are multiplied by the Yando geometric factors for each MEPED channel and integrated, referred to as $\int \mathrm{IDP}_{GF}$ for ease of reading (see the creation of simulated POES flux in Figure 1). These values represent the integral electron flux the POES/MEPED instrument would report assuming zero proton contamination.

5.2. A method for reversing the geometric factor effect

As the electron and proton fluxes are not correlated we must now examine the electron detection efficiency separately from the proton contamination. To calculate this efficiency we use all the electron flux data available from the DEMETER/IDP instrument which are measured outside the SAMA and the low flux equatorial regions. These excluded regions are discussed in Section 6.1 with conditions of L shell > 2.5 and 60° < longitude < 270°, giving 4.7 million non-zero data points for >30 keV and >100 keV integral energy fluxes. Of the available data approximately 75% also have a non-zero >300 keV integral energy flux. While the Yando geometric factors provide a multiplication factor to convert flux into counts, we require the opposite transformation. As the geometric factor is a set of discrete energy dependant values, finding the inverse function is not a simple exercise. Therefore, we compare the integral electron fluxes made from IDP to the differential electron fluxes multiplied by the Yando geometric factors and integrated, simulating the MEPED observations. Performing a fit between the unaltered and geometric factor multiplied electron fluxes provides a method of converting from uncorrected to corrected integral flux.

The results are shown in Figure 5, with the three panels showing the simulated E1, E2 and E3 respectively from top to bottom. The y-axis shows DEMETER integral flux values while the x-axis shows DEMETER differential fluxes multiplied by the Yando geometric factors and then integrated with respect to energy. Thus the x-axis should be equivalent to the POES integral uncorrected electron flux values after proton removal. The red dashed line shows the $y = x$ line and the black dash-dot line shows the best linear fit. The text on each plot is the best fit equation (linear fit on a $\log_{10}$ vs $\log_{10}$ plot) and is also listed below in Equations (4)-(6). The data in the top and central panels are described very well by a $y = x$ relation as shown by the red line in Figure 5, with the fitted spectral indicies having values very close to 1. The lower panel showing >300 keV integral fluxes has more variance from the $y = x$ line for integral fluxes less than 1000. The gradient of the fit line in this last panel is 1.29. While this is not as close to 1 as the previous two fits, the differences between the fitted line and the $y = x$ line are only significant at very low MEPED simulated fluxes. For example there is an order of magnitude difference between the y and x values at a POES simulated flux of 12 e.cm^{-2}sr^{-1}s^{-1}, with the difference between lines decreasing with increasing flux. The majority of the >300 keV scatter plot points have a POES simulated flux with values between 10^3 and 10^5 e.cm^{-2}sr^{-1}s^{-1}. The points which appear to deviate from the fit line are highlighted within the solid black lines in the >300 keV panel of Figure 5, containing points with an integral flux less than 1 e.cm^{-2}sr^{-1}s^{-1} and ranging from 1-3 orders of magnitude below the $y = x$ line. This area contains less than 20% of all data points and 38% of the data values between a simulated POES flux of 10 and 1000. Depending on the input electron spectrum the simulated POES E3 data (from an "assumed accurate" flux of 1 or less) can be as high as 700 electrons cm^{-2}sr^{-1}s^{-1}. The standard deviation for 10 to 100 simulated flux counts is around 15% and the standard deviation for the 100 to 700 simulated flux counts region is approximately 29%, suggesting that when the noise floor of 100 e.cm^{-2}sr^{-1}s^{-1} is returned by the POES E3 channel, the correction error will be significantly less than between 100 and 700. The frequency of values at higher fluxes means that this variance is not too important for the 90 degree detector. However, the 0 degree telescope will have a higher proportion of flux values in this less defined area around the noise floor. An interesting side effect of this relation is that when the DEMETER >300keV fluxes (as shown on the y-axis) are below a single flux unit the simulated POES E3 channel would typically report at least the noise floor level of 100 e.cm^{-2}sr^{-1}s^{-1}.

The best fit equations, summarized below, allow for a quick conversion from the integral IDP flux values multiplied by the geometric factors to those of the original IDP integral fluxes. The accuracy of these equations will be tested when comparing satellite spectra in Section 6.5.

$$E1_{IDP} = 1.95 \times E1_Y^{0.9589} \quad (4)$$

$$E2_{IDP} = 0.67 \times E2_Y^{1.023} \quad (5)$$

$$E3_{IDP} = 0.046 \times E3_Y^{1.288} \quad (6)$$

Where;
$E1_{IDP}$: is the integral E1 flux reported by the DEMETER satellite
$E1_Y$: is the simulated E1 flux, expected to be observed by

POES (assuming accurate proton contamination removal), and should thus represent the post-proton contamination E1 POES corrected electron flux.

Multiplying the MEPED flux by Equations (4)-(6), once the proton contamination is removed, will be hereafter referred to as MEPED_{GF} for ease of reading. Our approach should allow a non-contaminated electron flux reported by the POES satellites to be converted into what DEMETER would report, such that we can test the flux determination methods for both instruments.

$$MEPED \rightarrow -\text{protons} \rightarrow \times \text{ eqs(4) to (6)} \rightarrow \mathrm{MEPED_{GF}}$$

6. Satellite data comparisons

6.1. Criteria for matching spectra

Restrictions must be put in place to compare observations that are not only in similar locations but also unaffected by instrument noise or low fluxes. To remove the equatorial low fluxes the minimum L shell value of comparable spectra is set at L = 2.5. Longitudes between 270° (90°W) and 60° (60°E) are also not considered in this analysis as they contain the SAMA and its conjugate flux depletion in the northern hemisphere. The latitude difference between observation locations is also limited to no greater than 40° so that conjugate hemispheres are not compared. The remaining spectra are then subjected to the following conditions:

- The time between compared satellite spectra is less than 10 minutes.
- The longitude difference is less than 3°.
- The L shell difference is less than 0.5.

This results in over 9 million matches between the two satellites ranging from 23 May 2008 when the MetOp-2 mission data begins through to 3 January 2011 when the DEMETER mission ended. The number of matches per month increases with time from May 2008 until November 2010, when there is a sharp drop-off. This suggests the satellites were drifting together up to this point (POES satellite drift has been shown to exist in *Asikainen, Mursula and Maliniemi* [2012]) and so the most accurate values will come from 2010. To get a more manageable data set, only DEMETER orbit numbers 33xxx (spanning the time period; September 2010 to November 2010) are used which includes over 1.5 million conjunctions.

There are 3 main comparisons that we perform:

1. Examine the uncorrected MEPED values (counts x100) against $\int \mathrm{IDP}_{GF}$ (with our estimated proton contamination added). This will check whether our approach for producing synthetic POES data and proton contamination is valid, and is effectively testing the accuracy of the Yando geometric factor values. This is presented in Section 6.3).
2. Investigate the quality of the POES electron flux produced from the proton-corrected data using the equations in *Lam et al.* [2010] by comparing them against the IDP integral data. This will allow us to examine the validity of previous studies which used only the *Lam et al.* [2010] correction values but did not consider the energy dependent geometric factors described by *Yando et al.* [2011] The comparison is presented in Section 6.4).
3. Test the uncorrected MEPED data (after the proton contamination has been removed) multiplied by the equations in Section 5.2 against the IDP integral data. This takes into account both electron and proton geometric factors from *Yando et al.* [2011] on the POES spectra and will determine whether Equations (1)-(6) are accurate enough to use on a large scale for correcting the data easily. This will allow us to show how valid previous studies using only the Lam corrected values are. This is presented in Section 6.5).

These three tests are also described in the flow diagram of Figure 1.

6.2. Investigating a single case

An initial case study is performed to ensure that the processing is being performed correctly before moving onto the large scale comparisons and results. This particular case examines the electron spectrum seen by IDP on 18 November 2010 at 17:25:36 UT, chosen because it is in the outer radiation belt (L = 4.47), the low energy flux is high and the spectrum is relatively smooth. The equivalent MEPED electron spectrum is taken less than 6 minutes before this at an L-shell of 4.466, with a difference in longitude of 1.84°. Figure 6 shows these two spectra and the processing steps that are performed to create results for the full comparison data set.

Panel (a) of Figure 6 shows the IDP spectrum on a linear scale, with the black stars indicating all data points and the overplotted red stars indicating which points were included for the data fit shown by the blue line. The fitting was performed with a linear fit of the $\log_{10}$ of both the energy and flux values (the justification for this process is covered in *Whittaker et al.* [2013]). The fit does extremely well in describing the IDP data points on a linear set of axes with an r^2 value of 0.989. Panel (b) shows the next step which is to interpolate the IDP data between 10 keV and 10 MeV, shown in black on $\log_{10}$ axes. The red points and blue line are taken from panel (a). When the interpolation is performed the spectrum is cut off when it first drops below a flux of 1. We find this stops the interpolation from reproducing the false flux increases seen in the original data around 1.5 MeV. The interpolation does extend to 10 MeV but as this plot is on logarithmic axes zero values are not shown. Panel (c) shows the interpolated IDP data (in black) multiplied by the interpolated geometric factor values in *Yando et al.* [2011] for each integral channel (E1 in red, E2 in blue and E3 in green). The channel curves show some flux continuation from electrons below 30 keV will be included in the E1 ">30 keV channel" and electrons below 300 keV in the ">300 keV channel", while the E2 channel cutoff value of 100 keV is strict. Panel (d) of Figure 6 shows the MEPED uncorrected integral flux values (i.e. counts x100, in red) for 18 November 2010 at 17:19:53 at an L shell of 4.466. In contrast the black values show the interpolated IDP_{GF} data, calculated by summing each IDP flux channel in panel (c) and adding the proton contamination calculated from the MEPED data using Equations (1)-(3). The values for E1 and E2 have a similar offset in flux, however, the E3 channel results are closer together. The simulated MEPED values (from IDP) have a mean difference of 13.8% from the uncorrected MEPED values. In panel (e) the integrated IDP fluxes from panel (b) are shown in red and the black line shows the integral fluxes found using the *Lam et al.* [2010] algorithm, i.e., corrected for proton contamination but not the energy response. The blue line in panel (e) shows the integral fluxes determined from the POES data after the application of Equations (1)- (6), i.e., allowing for the energy response and the proton contamination. The three lines in this panel show very similar values with a mean difference of 13% (Lam corrected) and 15% (Yando corrected) from the integral IDP values. Note that the proton contamination fluxes for this spectrum were determined to be 757 $\mathrm{e.cm^{-2}sr^{-1}s^{-1}}$ for E1, 331 for E2 and 91 for E3 and hence, are small compared to the data values. The black line in panel (*e*) (POES Lam proton correction only) has essentially the same values as the black line in panel (*d*) which is the uncorrected POES data (i.e. geometric factor of 100), suggesting that the estimate of small proton contamination is accurate. The final panel, (*f*), shows the differential flux fits. The original IDP data is shown by the black line on $\log_{10}$ axes, the fit to this original data is shown as the blue line through the data (as in panels (*a*) and (*b*)). The green line in this panel is produced by differentiating a line which was fitted to the MEPED_{GF} data points in panel (*e*). Note that this fit line is very close to the IDP fit and describes the data very well, suggesting that in this case the POES data can be used to reasonably reproduce the DEMETER high-energy resolution differential flux distribution. As a further test the integral IDP data (red line in panel (*e*)) is fitted and then differentiated. The resulting line is shown in red in panel (*f*)). The low energy values are very similar while the fit is less accurate at the highest energy values (> 1 MeV).

The extrapolation of the DEMETER electron data in panel (*c*) down to 10 keV allows us to investigate how much this interpolation of the data affects the simulated >30 keV flux. The 10-19 keV flux comprises 0.005% of the total simulated MEPED > 30 keV flux, the 20-29 keV flux adds another 0.5% of the total flux and the rest of the interpolated energy (30-72 keV) provides 14.6% of the total flux. Thus 15.1% of the total simulated MEPED >30 keV flux is due to electrons in the range of the extrapolated data, suggesting a small error in the interpolation will make little difference to the integral electron fluxes. The values in panel (*e*) show that the Lam proton correction method produces fluxes with values of 82%, 94% and 115% of the integral DEMETER IDP fluxes. The values for the Yando geometric factor produce fluxes of 103%, 80% and 80% of the DEMETER integral IDP flux, which shows that the Yando geometric factor produces the closest fluxes to DEMETER for E1 and the Lam fluxes are closer for E2 and E3. In panel (*f*), we see that the fit equations for the Yando differential flux show a similar gradient to the DEMETER fit of panel (*a*). The fit lines meet at an energy of 2.05 MeV with a flux of 0.0121 $\text{e.cm}^{-2}\text{sr}^{-1}\text{s}^{-1}$ and at 30 keV the Yando flux is 46% that of the DEMETER flux. These differences are quite small when the flux at 30 keV is 5 orders of magnitude large than the 2.05 MeV flux. These comparisons show that the methods for converting between data types are fairly successful (within an approximate factor of 2) in this case and have been applied accurately. We now move on to applying these processes to the full set of data comparisons.

6.3. Simulated MEPED values against uncorrected MEPED data

The IDP data restrictions used for this comparison were described in Section 5.1. After having been multiplied by the values given in *Yando et al.* [2011] and integrated, the proton contamination is then added to each of the integral fluxes. The three channels are then compared to the MEPED uncorrected fluxes (counts x100), as described in Figure 1. The results of this can be seen in the left panels of Figure 7, which illustrates the relation with a binned frequency plot.

The top panel of Figure 7 shows the E1 relation and the middle panel shows the E2 relation. Although there is a wide spread, the highest scatter point density bins are well described by $y = x$. Comparing these high occurrence areas to the black solid line (showing $y = x$) it is clear that the altered IDP values do a reasonable job of approximating the MEPED E1 and E2 channels. The lower panel of Figure 7 shows the simulated and observed E3 channel. The high occurrence linear relationship is not as clear but the general trends still appear to agree with the $y = x$ line. Table 1 shows the r^2 value for this relation on each scatter plot. While the frequency plots in Figure 7 are shown on a $\log_{10}$ flux scale, the fits have been performed on a linear scale.

As previously described in Section 3 both satellites are not flying at the same altitude, so it is unlikely that the fluxes would be exactly the same, even when both satellites sample the same field line. To test this theory, r^2 values are found for a range of modified $\int \text{IDP}_{GF}$ values. Rather than applying a constant flux difference, a percentage change of the simulated MEPED values are applied to all data points until a maximum r^2 value is found. The results of this are also listed in Table 1 along with the optimum r^2 that these changes return. Examining the optimum flux differences shows that the IDP simulation of MEPED overestimates the MEPED flux values by an average factor of 42%. When these differences are applied, the r^2 values become very high. This overestimation is likely to be due to the areas sampled, for example Figure 2 shows that in the inner belt DEMETER sees higher flux than POES (possibly due to the pitch angle particle distribution at different altitudes discussed in Section 3.2).

As the $y = x$ correlations are performed on linear data sets, the small amounts of MEPED flux $>10^6$ $\text{e.cm}^{-2}\text{sr}^{-1}\text{s}^{-1}$ in the E1 comparison may be a strong factor in r^2 determination. Without these very high fluxes the linear $y = x$ line should return a better r^2 fit value. The r^2 optimization was performed again for each integral energy channel within the MEPED flux range of $10^{2.5}$ to $10^{5.5}$ to determine if very high or very low fluxes affected the $y = x$ fit. The r^2 values increased slightly but the overestimation of the highest occurrence values by the $y = x$ line changed by less than 2% in each case. The y = mx fit has also been performed for comparative purposes and is shown as the dash-dot green line on each plot. The gradients are all close to 0.5, an expected result with the flux differences in Figure 2 being around a factor of 2 higher in DEMETER. The gradients are also listed in Table 1.

From this comparison we conclude that the geometric factors determined by Yando's modeling of the POES/MEPED instrument brings the flux values closer to those derived from DEMETER measurements. Our Equations (1)-(3) describing proton contamination have also shown to be valid.

6.4. Lam corrected MEPED data against integral IDP

We now compare the MEPED data corrected by the equations in *Lam et al.* [2010] against the unmodified integral IDP data. As seen in the previous section the application of the Yando geometric factors to the IDP data produces a reasonable simulation of the uncorrected MEPED fluxes. If the Lam proton-corrected electron fluxes are accurate then it should match up to the unmodified integral IDP data in a similar way to the results of the previous section.

The results from this comparison are shown in the right panels of Figure 7 to allow for direct comparison with the results of Section 6.3. The top right plot shows the *Lam et al.* [2010] corrected E1 values on the x-axis against the >30 keV integral IDP data on the y-axis. This panel looks very similar to the top left panel. The $y = x$ line goes through most of the high occurence areas although it also appears to slightly underestimate the position of the integral IDP high frequency bins, which was not evident for the case of the simulated against uncorrected MEPED data in the previous section. The middle right panel shows the proton corrected E2 values. This panel again shows similarities with the equivalent left hand panel, with the $y = x$ line going through almost the same bins. The lower right panel has less visible noise value columns and fewer values with an IDP integral flux < 1. In a similar manner to Section 6.3 the r^2 values, optimum flux change with new r^2 values and the y = mx fit are listed in Table 1. The optimum r^2 fit with a linear gradient of 1 requires an average 54% flux change in this case. This is marginally higher than the application of the geometric factor to the IDP data case, although does return better fits in the E2 and E3 channels. This is also reflected in the gradient fit with the E1 relation having a slightly higher gradient than the E2 or E3 channels.

From this comparison we conclude that the equations from *Lam et al.* [2010] are acceptable for approximating the DEMETER data from a POES flux, This suggests previous work which has used this method of data correction took a valid approach.

6.5. Yando corrected MEPED data against integral IDP

The Yando geometric factor transformation from Section 5.2 is now tested by applying these equations (as well as the proton removal described in Section 4) to the uncorrected MEPED flux data (see the definition in Section 3.1). These fluxes can then be compared to the IDP integral data, essentially reversing the test we undertook in Section 6.3. If the results of this comparison are similar to Section 6.3 we will conclude we have validated Equations (1) to (6). Recall these equations were based on the geometric factors reported by *Yando et al.* [2011], and reverse the energy dependent detection efficiencies.

The results of the comparison are shown in the left panels of Figure 8 with the MEPED$_{GF}$ values along the x axis and the integral IDP data along the y axis. The $y = x$ line is again placed on these frequency plots to assist in the comparison with the left panels of Figure 7. Visually the plots in E1 and E2 (upper and middle panels) look very similar to Figure 7, while there are slightly more significant differences in the case of E3. These differences mainly show that the equations in Section 5.2 do not recreate the IDP flux values lower than 1 flux unit, produced when the Yando geometric factors are applied to the very low-flux IDP data. In comparison to Section 6.3 the corrected E3 fluxes from POES are much closer to approximating DEMETER than DEMETER can simulate POES E3 observations, as seen by the higher r^2 values seen in Table 1. This is because Equation (6) mostly ignores the wide data spread in the black box in the lower panel of Figure 5 by the application of the Yando geometric factors to very low fluxes and hence this gives a more accurate simulation.

The r^2 values for each channel are shown in Table 1. As with the visual inspection the r^2 values of the $y = x$ line are similar to the results in Section 6.3 in E1 and E2 with a much higher r^2 in E3. The latter point can be explained by the lower number of data values below 1 seen in the lower panel of Figure 8. To get the optimum fit with a linear gradient of 1 the percentage change for E2 is exactly the same as in Section 6.3 suggesting that Equation (5) is very accurate in describing the *Yando et al.* [2011] geometric factor conversion. The E1 values produced by Equation (4) give a very close initial r^2 value to the E1 comparison from Section 6.3 and only a small flux change difference is required to get an optimum value when compared to the maximum flux difference of 200% between satellites from Figure 2. As described above the E3 values produced by Equation 6 have a different initial r^2 value from the E3 comparison in Section 6.3 but this is caused by the lack of DEMETER integral electron flux below 1 e.cm^{-2}sr^{-1}s^{-1} which, as seen in the lower panel of Figure 8, actually improves the simulation. This better r^2 value suggests that the scatter bounded by the black box in the E3 panel of Figure 5 is not real. If required anyone wishing to use Equations (4), (5) and (6) may choose to ignore the small number of POES spectra with E3 flux values less than 700 flux units (i.e. 7 counts). This would eliminate the low flux variability completely.

The y = mx fit line (green dash-dot) is also shown on each plot and the gradient can now be used as another method of comparing the accuracy of Equations (1)-(6). Examining Table 1, E1 and E2 show a very strong similarity between the DEMETER simulation of POES flux against uncorrected POES flux (0.5531 and 0.6205) and the gradient of the fit of the geometric factor corrections multiplied by the POES data compared to DEMETER (0.5838 and 0.6093). This similarity indicates that the reversal of the Yando geometric factors has been performed accurately. The E3 channel does show a difference between the two comparisons however. The DEMETER simulation of POES shows a slightly sharper gradient due to the flux values below 1 e.cm^{-2}sr^{-1}s^{-1}. The POES E3 values multiplied by the correction factors in Equations (3) and (6) produces a fit gradient (0.4228) very close to that of the Lam E3 gradient (0.4226). As we have already shown that the Lam values are very close to the Yando values we can assume that Equation (6) is also accurate.

From this comparison we have validated Equations 1-6 as an accurate way of correcting the POES data for both proton contamination and electron detection efficiency.

6.6. Spectral index fit comparisons

As a final test, the spectral indicies fitted to the integral flux calculated from DEMETER data and the corrected POES integral fluxes are also compared. This is shown in the top right panel of Figure 8 with a frequency occurrence plot. The black solid line shows the y = x relation and the green dash-dot line shows the linear y = mx best fit to the data. If the integral fluxes of DEMETER and POES are the same after the reversal of the geometric factors then their spectral indicies should also be the same. The highest occurrence bins sit very close to the y = x line (black) and the optimal r^2 is achieved with an offset of +0.404. The green best fit line indicates that the DEMETER spectral indicies are on average 0.75 that seen by POES. The best fit of these three lines is the gradient of 1 with an offset of 0.404. The adjusted r^2 value for this line is 0.136, with 964438 data points fitted, this r^2 value is well above the 99.9% confidence level.

The lower right panel of Figure 8 is a global median map of MEPED differential flux power-law spectral index values (integral spectral index - 1), this shows the values closer to zero at the polar edge of the spatial bands analyzed, relating to the outer radiation belt. The more strongly negative spectral index values occur in the inner radiation belt. The differential spectral indicies are shown here to allow a direct comparison to the DEMETER spectral index maps shown in *Whittaker et al.* [2013]. The spectral indicies in this study match up very well those in *Whittaker et al.* [2013], with the inner belt having an average spectral index around -4 and the slot and outer belt having an average spectral index around -2.

Previous studies using POES have also made use of the P6 channel (protons >6.9 MeV) of the MEPED instrument as a monitor for relativistic electron observations [e.g *Miyoshi et al.*, 2008; *Sandanger et al.*, 2009; *Rodger et al.*, 2010b; *Millan et al.*, 2010]. However, our study does not include this channel as relativistic electrons will produce very low fluxes and hence, any errors in this P6 value could significantly impact the fit coefficients.

7. Conclusions

This study has focused on showing the similarities and differences between the DEMETER IDP electron fluxes and the POES/MetOp-2 MEPED integral energy electron data. The comparison was undertaken when both instruments were in similar orbits, such that they were measuring similar electron counts at the same time and place. We find that the median flux maps for the two instruments in the same time period are almost identical (as shown in Figure 2), validating the basis for this comparison.

The *Yando et al.* [2011] geometric factors, which take into account electron detection efficiencies and proton contaminations in the electron telescopes, were used to simulate the MEPED observations from the higher resolution and more accurate DEMETER IDP measurements. When trying to reverse this there are multiple different potential differential flux spectra which result in the same POES 3 value (>30, >100 and >300 keV) integral spectrum. The effect of the geometric factor values have been directly applied to the DEMETER electron flux data and the differences to the integral energy channels were examined. This application of the geometric factors allowed a set of equations to be developed which describe how to reverse the geometric factor effect on each integral energy channel of the MEPED electron flux data.

In a similar manner, the effect of protons producing false "contamination" observations in the electron telescope of the MEPED instrument were investigated by using the proton data supplied by the MEPED instrument. This gives very specific spectral shapes at different *L*-shells which allows representative proton removal formulae to be calculated based on the appropriate proton power law spectral index for each electron flux spectrum. These equations show, on average, a $\sim$700 e.cm^{-2}sr^{-1}s^{-1} flux increase in E1, 300 e.cm^{-2}sr^{-1}s^{-1} flux increase in E2 and 100 e.cm^{-2}sr^{-1}s^{-1} for E3 in the radiation belts. This contamination, while stable under quiet conditions, does change in strongly disturbed geomagnetic conditions.

The comparison of integral electron fluxes from both the IDP and MEPED instruments shows striking similarities. This is true not only for the Yando geometric factor values when applied to the IDP instrument (Section 6.3), but also the application of the *Lam et al.* [2010] correction equations to the POES data (which focus on proton contamination removal; Section 6.4). The Yando geometric factors were shown to be very accurate in reproducing MEPED electron flux from the IDP integral data, with r^2 values around 0.8 for a $y = x + c$ fit. While the Lam equations are not as accurate as the Yando geometric factor values, the single orbit case in Figure 6 and comparisons in Figures 7 and 8 all show that the differences are minor. Table 1 also quantitatively shows this similarity between methods with the optimal fitting constant added to the $y = x$ fit line being very similar for each energy channel, validating previous work which relied upon the Lam correction approach.

The results of Table 1 also provide some insight into the pitch angle dependence of electrons at different altitudes. As we take comparisons between the two instruments at very small time differences we can assume that an equal IGRF L shell will correspond to an equal L* (an L shell value which varies with geomagnetic currents) value. This means that the phase space density (PSD), which is conserved along a field line, should be equal for both satellite data points [*Chen et al.*, 2007]. As PSD is a function of μ, K and L* which in turn are functions of pitch angle, particle energy, magnetic field strength and L* then this can provide information on the most likely pitch angle of electrons at these different altitudes. This sort of information for each integral energy range could be used as important verifications and tests for modelling codes such as DREAM (Dynamic Radiation Environment Assimilation Model) [*Reeves et al.*, 2012].

The equations given in our study to reverse the geometric factor energy dependent detection efficiency (expressed by geometric factor) on the MEPED instrument have been shown in Section 6.5 to work very well. The comparison between these corrected fluxes to integral IDP data (Figure 8) also shows a strong similarity to the comparison of IDP electron flux multiplied by the Yando geometric factor against uncorrected MEPED data (Figure 7). This means that Equations (1)-(6) which we have developed in this study are a valid and appropriate approach to correcting for the geometric factor in the MEPED electron flux instrument.

Acknowledgments. The research leading to these results has received funding from the European Community's Seventh Framework Programme ([FP7/2007-2013]) under grant agreement number 263218. The authors wish to thank the NOAA personnel who developed, maintain, and operate the NOAA/POES spacecraft. The data used in this paper are available at NOAA's National Geophysical Data Center (NGDC - MetOp-02 MEPED data) and CNES/CESR Centre de Donnees pour la Physique des Plasmas (CDPP - for DEMETER IDP data) for all years of operation.

References

Asikainen, T., K. Mursula and V. Maliniemi (2012), Correction of detector noise and recalibration of NOAA/MEPED energetic proton fluxes, *J. Geophys. Res.*, *117*(A09204), doi:10.1029/2011JA017593.

Asikainen, T., and K. Mursula (2013), Correcting the NOAA/MEPED energetic electron fluxes for detector efficiency and proton contamination, *J. Geophys. Res.*, *116*(A10231), doi:10.1029/2011JA016671.

Brasseur, G., and S. Solomon (2005), *Aeronomy of the Middle Atmosphere, third ed.*, D. Reidel Publishing Company, Dordrecht.

Callis, L. B. (1997), Odd nitrogen formed by energetic electron precipitation as calculated from TIROS data, *Geophys. Res. Lett.*, *24*(24), doi:10.1029/97GL03276

Carson, B., C. J. Rodger and M. A. Clilverd (2013), POES satellite observations of EMIC-wave driven relativistic electron precipitation during 1998-2010, *J. Geophys. Res.*, *118*, doi:10.1029/2012JA017998.

Chen, Y., R. H. W. Friedel, G. D. Reeves, T. E. Cayton, and R. Christensen (2007), Multisatellite determination of the relativistic electron phase space density at geosynchronous orbit: An integrated investigation during geomagnetic storm times., *J. Geophys. Res.*, *112*(A11214), doi:10.1029/2007JA012314.

Evans, D. S., and M. S. Greer (2004), Polar orbit environmental space satellite space environment monitor 2: Instrument description and archived data documentation v1.3, *NOAA Technical Memorandum, Space Environ. Lab., Boulder, Colorado*

Galand, M., and D. S. Evans (2000), Radiation damage of the proton MEPED detector on POES(TIROS/NOAA) satellites, *NOAA Technical Memorandum OAR 456-SEC 42, Space Environ. Lab., Boulder, Colorado*

Gamble, R. J. (2011), The 17-19 january 2005 atmospheric electron precipitation event., Ph.D. thesis, department of Physics, University of Otago.

Green, J. C. (2013), MEPED telescope data processing theoretical basis document version 1.0, *NOAA Technical Memorandum*, *Space Environ. Lab., Boulder, Colorado*

Lam M. M., R. B. Horne, N. P. Meredith, S. A. Glauert, T. Moffat-Griffin and J. C. Green (2010), Origin of energetic electron precipitation >30 keV into the atmosphere., *J. Geophys. Res.*, *115*(A00F08), doi:10.1029/2009JA014619.

Li W., B. Ni, R. M. Thorne, J. Bortnik, J. C. Green, C. A. Kletzing, W. S. Kurth and G. B. Hospodarsky (2013), Constructing the global distribution of chorus wave intensity using measurements of electrons by the POES satellites and waves by the Van Allen Probes., *Geophys. Res. Lett.*, *40*(17), doi:10.1002/grl.50920.

Meredith, N. P, R. B. Horne, M. M. Lam, M. H. Denton, J. E. Borovsky and J. C. Green (2011), Energetic electron precipitation during high-speed solar wind stream driven storms., *J. Geophys. Res.*, *116*(A05223), doi:10.1029/2010JA016293.

Millan, R. M, K. B. Yando, J. C. Green, and A. Y. Ukhorskiy (2010), Spatial distribution of relativistic electron precipitation during a radiation belt depletion event., *Geophys. Res. Lett.*, *37*(L20103), doi:10.1029/2010GL044919.

Miyoshi, Y, K. Sakaguchi, K. Shiokawa, D. S. Evans, J. Albert, M. Conners and V. Jordanova (2008), Precipitation of radiation belt electrons by EMIC waves, observed from ground and space., *Geophys. Res. Lett.*, *35*(23), doi:10.1029/2008GL035727.

Newnham, D. A., P. J. Espy, M. A. Clilverd, C. J. Rodger, A. Seppälä, D. J. Maxfield, P. Hartogh, K. Holmén, and R. B. Horne (2011), Direct observations of nitric oxide produced by energetic electron precipitation in the antarctic middle atmosphere, *Geophys. Res. Lett.*, *38*(20), L20,104, doi:10.1029/2011GL049199.

Randall, C. E, V. L. Harvey, G. L. Manney, Y. Orsolini, M. Codrescu, C. Sioris, S. Brohede, C. S. Haley, L. L. Gordley, J. M. Zawodny, and J. M. Russell III (2005), Stratospheric effects of energetic particle precipitation in 20032004., *J. Geophys. Res.*, *32*(L05802), doi:10.1029/2004GL022003.

Reeves, G. D., Y. Chen, G. S. Cunningham, R. W. H. Friedel, M. G. Henderson, V. K. Jordanova, J. Koller, S. K. Morley, M. F. Thomsen, and S. Zaharia (2012), Dynamic Radiation Environment Assimilation Model: DREAM., *Space Weather*, *10*(S03006), doi:10.1029/2011SW000729.

Rodger, C. J., B. Carson, S. Cummer, R.J. Gamble, M. Clilverd, J. Green, J.-A. Sauvaud, M. Parrot, and J.-J. Berthelier (2010a), Contrasting the efficiency of radiation belt losses caused by ducted and nonducted whistler-mode waves from ground-based transmitters., *J. Geophys. Res.*, *115*(A12208), doi:10.1029/2010JA015880.

Rodger, C. J., M. A. Clilverd, J. Green, and M. Lam (2010b), Use of poes sem2 observations to examine radiation belt dynamics and energetic electron precipitation in to the atmosphere, *J. Geophys. Res.*, *115*, A04,202, doi:10.1029/2008JA014023.

Rodger, C. J., A. J. Kavanagh, M. A. Clilverd, and S. R. Marple (2013), Comparison between POES energetic electron precipitation observations and riometer absorptions; implications for determining true precipitation fluxes *J. Geophys. Res.*, doi: 10.1002/2013JA019439

Sandanger, M. I., F. Søraas, M. Sørbø, K. Aarsnes, K. Oksavik, and D. S. Evans (2009), Relativistic electron losses related to EMIC waves during CIR and CME storms., *J. Atmos. sol-terr. phys.*, *71*(10-11), doi:10.1016/j.jastp.2008.07.006.

Sauvaud, J.-A, T. Moreau, R. Maggiolo, J. Treilhou, C. Jacquey, A. Cros, J. Coutelier, J. Rouzard, E. Penou, and M. Gangloff (2006), High-energy electron detection onboard demeter: The IDP spectrometer, description and first results on the inner belt., *PSS*, *54*(5), doi:10.1016/j.pss.2005.10.019.

Selesnick, R. and J. Blake (2000), On the source location of radiation belt relativistic electrons, *J. Geophys. Res.*, *105*, doi:10.1029/1999JA900445.

Solomon, S., P. J. Crutzen, and R. G. Roble (1982), Photochemical coupling between the thermosphere and the lower atmosphere: 1. Odd nitrogen from 50 to 120 km, *J. Geophys. Res.*, *87*, doi:10.1029/JC087iC09p07206.

SPIDR data archive, NGDC/NOAA (2013), Geomagnetic indicies, retrieved February 1, 2013, from http://spidr.ngdc.noaa.gov/spidr/basket.do

Space Weather Prediction Center, NOAA (2011), The k-index, retrieved February 1, 2013, from http://www.swpc.noaa.gov/info/Kindex.html.

Tan, L. C., S. F. Fung, and X. Shao (2007), NOAA-5 to NOAA-14 Data Reprocessed at GSFC/SPDF. *NASA Space Physics Data Facility: NOAA/POES MEPED Data Documentation.*

Thorne, R. M. (2010), Radiation belt dynamics: The importance of wave-particle interactions, *Geophys. Res. Lett.*, *37*(22), doi:10.1029/2010GL044990.

Tsurutani, B. T., and G. S. Lakhina (1997), Some basic concepts of wave-particle interactions in collisionless plasmas, *Rev. Geophys.*, *35*(4), 491501, doi:10.1029/97RG02200.

Turner, D. L., Y. Shprits, M. Hartinger, and V. Angelopoulos (2012), Explaining sudden losses of outer radiation belt electrons during geomagnetic storms., *Nature Physics*, *8*(3), doi:10.1038/NPHYS2185.

Turunen, E., P. T. Verronen, A. Seppälä, C. J. Rodger, M. A. Clilverd, J. Tamminen, C. F. Enell, and T. Ulich (2009), Impact of different energies of precipitating particles on nox generation in the middle and upper atmosphere during geomagnetic storms, *J. Atmos. Sol. Terr. Phys.*, *71*, 1176–1189, doi:10.1029/2002GL016513.

Verronen, P. T., C. J. Rodger, M. A. Clilverd, and S. Wang (2011), First evidence of mesospheric hydroxyl response to electron precipitation from the radiation belts, *J. Geophys. Res.*, *116*(D07307), doi:10.1029/2010JD014965.

Whittaker, I. C., R. J. Gamble, C. J. Rodger, M. A. Clilverd and J.-A. Sauvaud (2013), Determining the spectra of radiation belt electron losses: Fitting DEMETER IDP observations for typical and storm-times, *J. Geophys. Res.*, doi:10.1002/2013JA019228

Wissing, J. M, and M.-B. Kallenrode (2009), Atmospheric Ionization Module Osnabruck (AIMOS): a 3-D model to determine atmospheric ionization by energetic charged particles from different populations., *J. Geophys. Res.*, *114*(5), doi:10.1029/2008JA013884.

Yando, K., R. M. Millan, J. C. Green, and D. S. Evans (2011), A Monte Carlo simulation of the NOAA POES Medium Energy Proton and Electron Detector instrument, *J. Geophys. Res.*, *118*, doi:10.1002/jgra.50584

Corresponding author: I. Whittaker, Department of Physics, University of Otago, PO Box 56, Dunedin 9054, New Zealand. (ian.whittaker@otago.ac.nz)

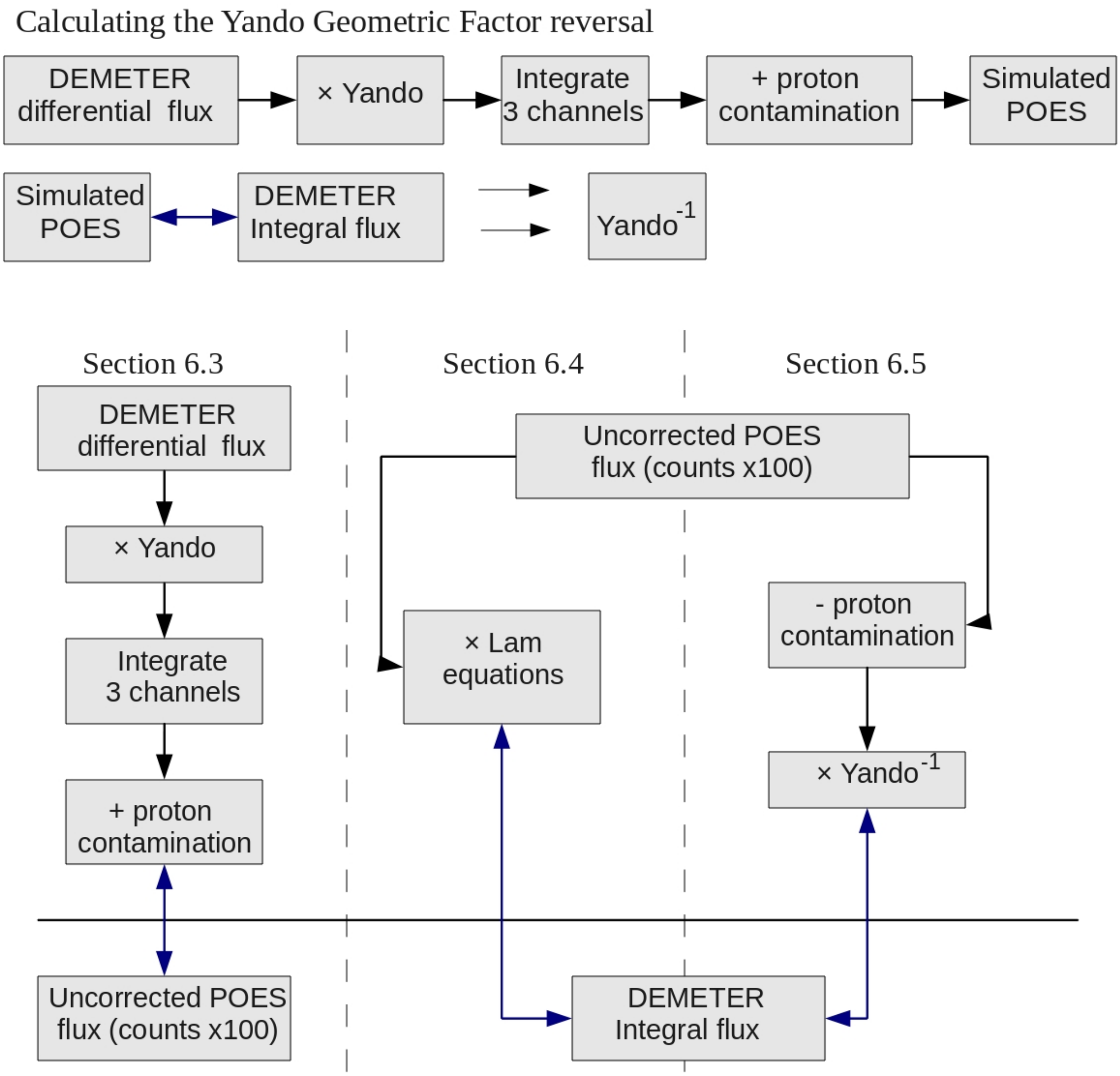

Figure 1: *Flow diagram showing the data processing used to create the variables for comparison. Black arrows show a process and blue double arrows indicate a comparison. The top line shows how we create a simulated POES energy spectrum from DEMETER data (Section 5.1), this is then compared with DEMETER integral flux (blue double arrow) to produce (twin black arrow) Equations (4),(5) and (6) in Section 5.2. The three comparisons used to determine the accuracy of each correction method are shown under their respective manuscript section heading.*

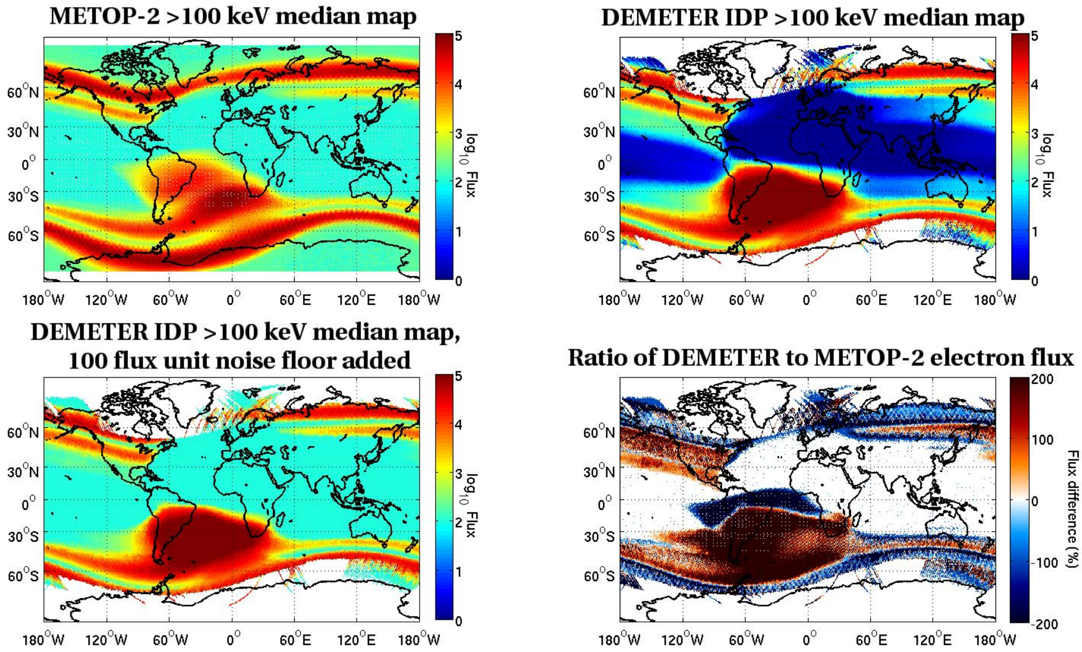

Figure 2: *Global median flux maps showing MetOp-2 MEPED >100 keV electron fluxes from the 90° E2 detector (top left panel) and DEMETER IDP >100 keV electron fluxes (top right panel). The units for both maps are on a* log_{10} *scale in* $e.cm^{-2}sr^{-1}s^{-1}$. *The lower left plot reproduces the DEMETER IDP data but the minimum data value is set at 100 flux units to mimic the MEPED noise floor. The lower right plot shows the ratio of the lower left hand panel adjusted DEMETER to the upper left panel MEPED observations, with the difference given as a percentage of the IDP flux.*

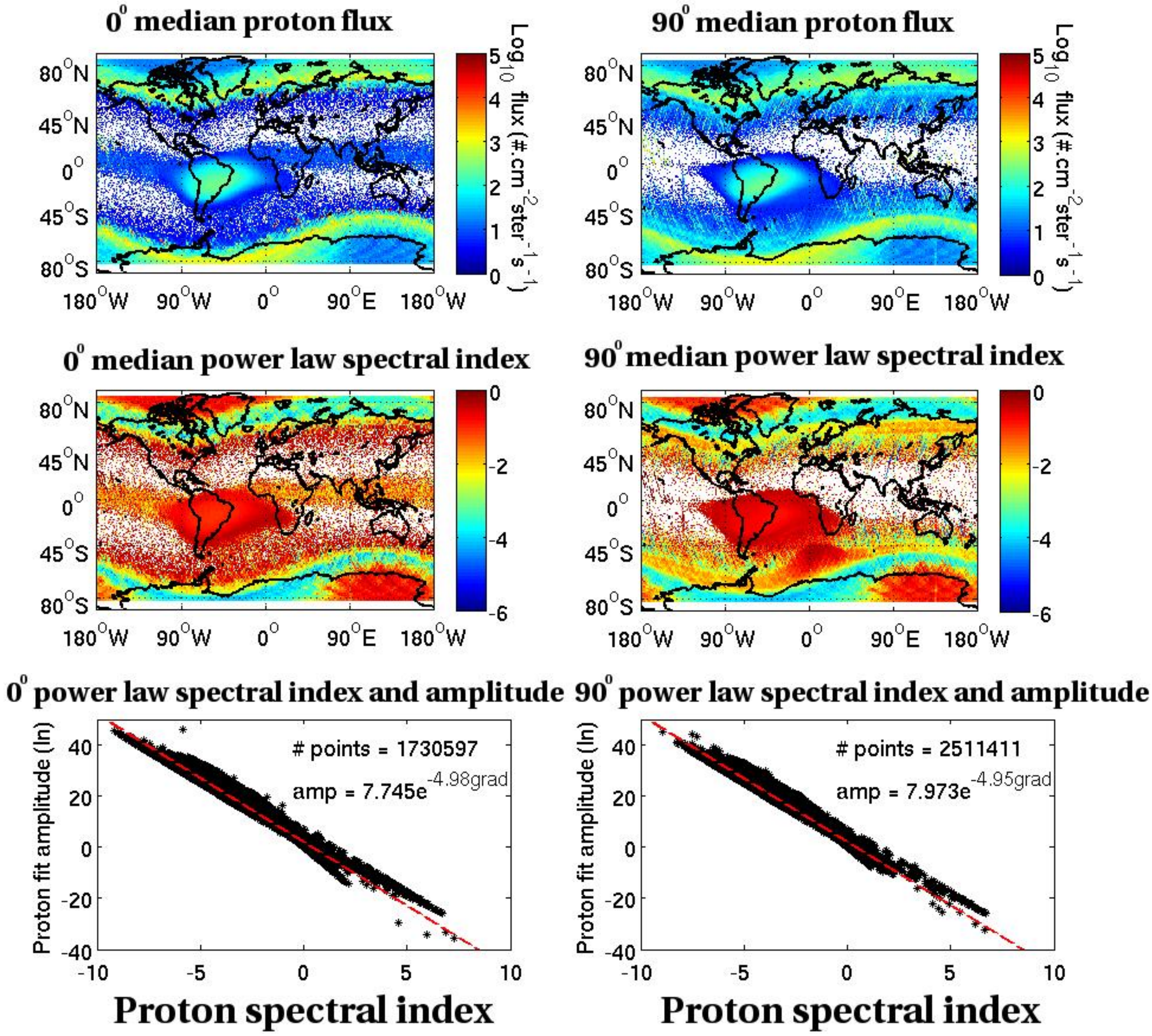

Figure 3: *Top: Global median >30 keV proton flux maps taken from NOAA 15-19 and MetOp-2 in January 2012 with a resolution of 1°. Middle: Global median proton power law spectral index maps. Lower: Scatter plots showing the relation between proton spectral index and amplitude. The left side shows the response from the 0° detector and the right panels show the 90° response. The flux values in the upper panels are on a* log_{10} *color scale.*

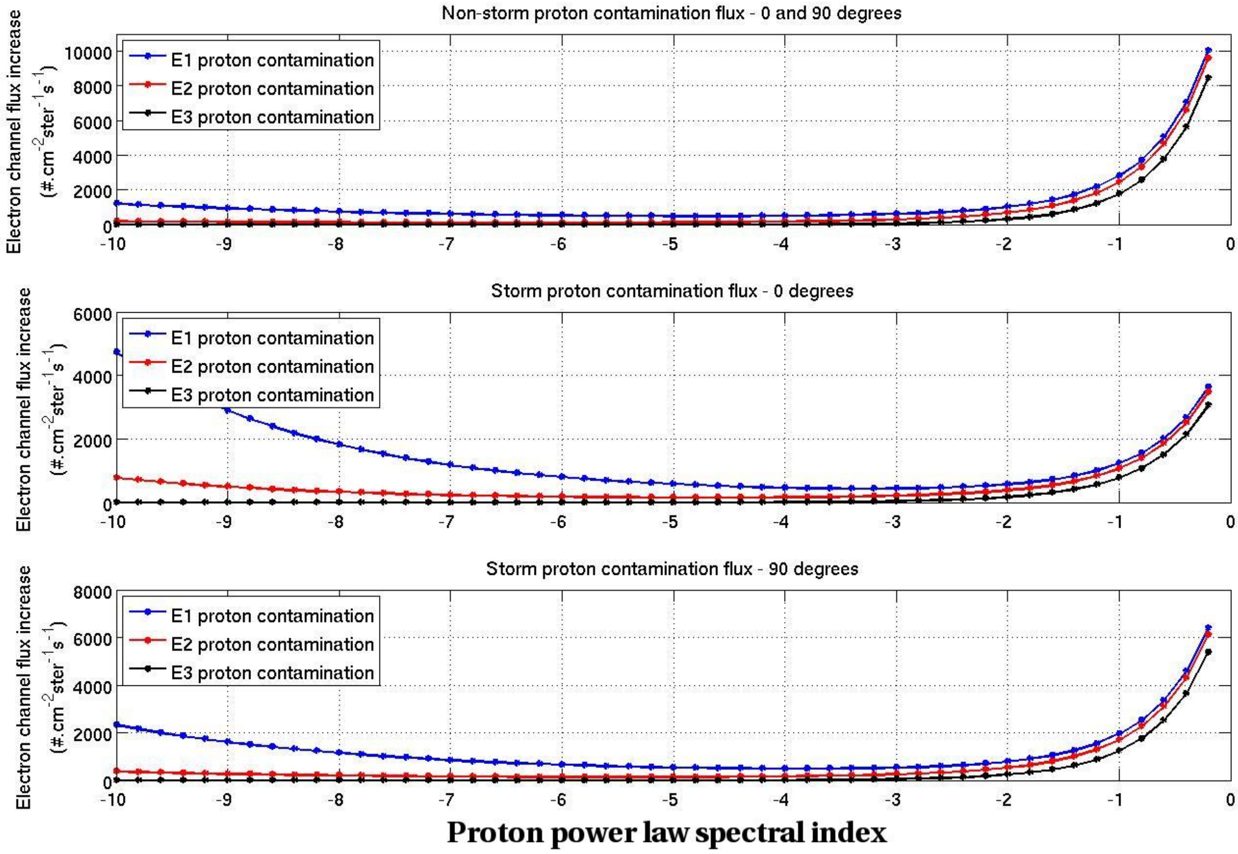

Figure 4: *The proton contamination flux values present in each electron integral flux channel based on the proton fit spectral index. This simplification is possible because of the high correlation of the exponential fit to fitted spectral index and amplitude values seen in Figure 3. (Top) The proton contamination flux average values for both 0 and 90 degree detectors. In this case the contamination of E2 and E3 are almost zero for a proton spectral index smaller than -3. (Middle) The 0 degree detector proton contamination flux during geomagnetic storm times (Kp > 5.3). (Bottom) The storm-time 90 degree proton contamination in the electron fluxes reported.*

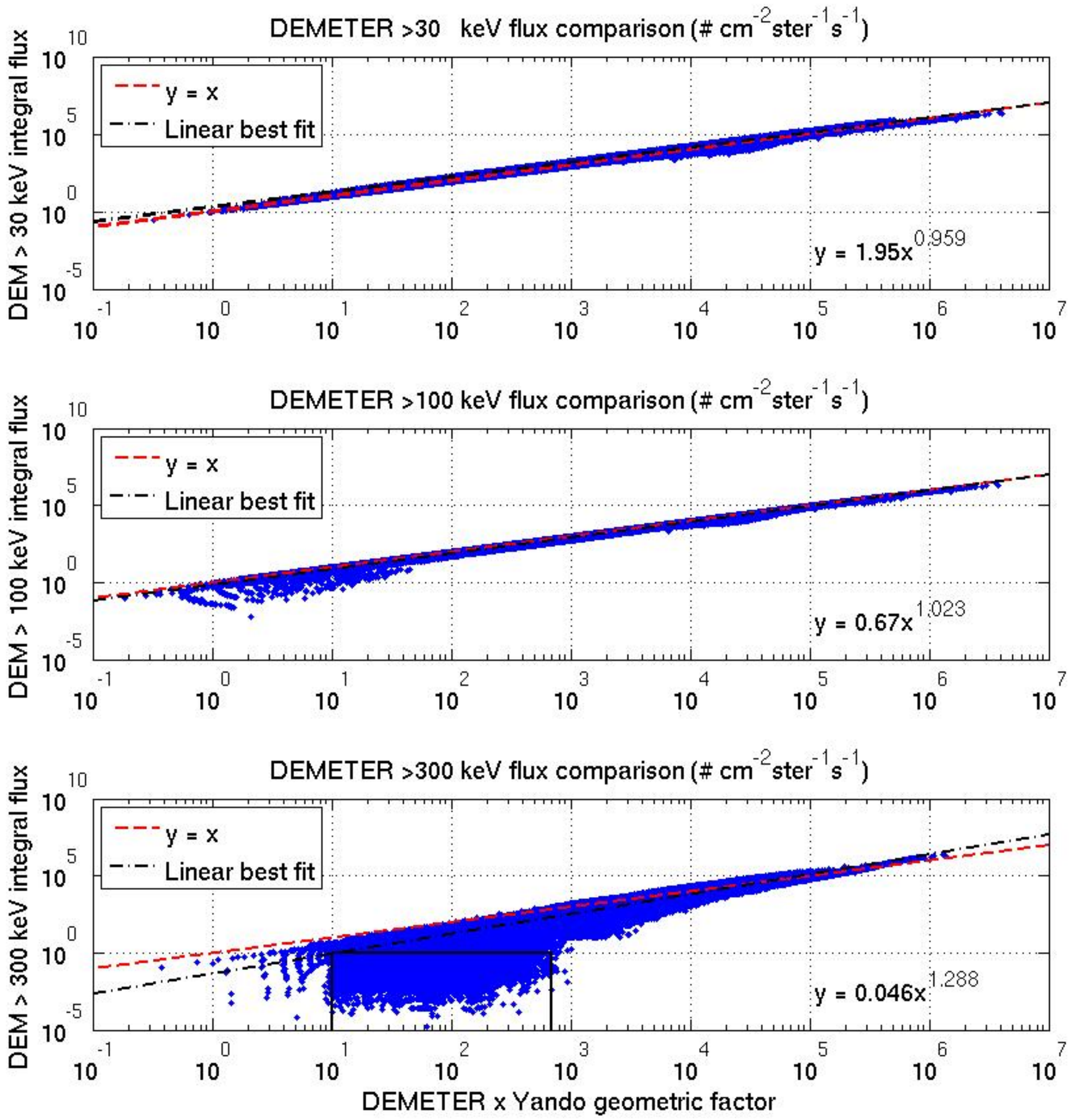

Figure 5: *Three scatter plots showing the comparison between the integral DEMETER data multiplied by the Yando geometric factor (x-axis) to integral DEMETER data with no modifications (y-axis), for the energy ranges >30 keV (top panel), >100 keV (middle panel) and >300 keV (lower panel). The red dashed line shows the* $y = x$ *line while the black dash-dot line shows the linear fit. The best fit line is very similar to the* $y = x$ *line in the upper two panels, while a slight deviation can be seen in the >300 keV channel. The scatter plots contain 4.7 million data points for >30 keV and >100 keV and 3.5 million (non-zero) fluxes for >300 keV.*

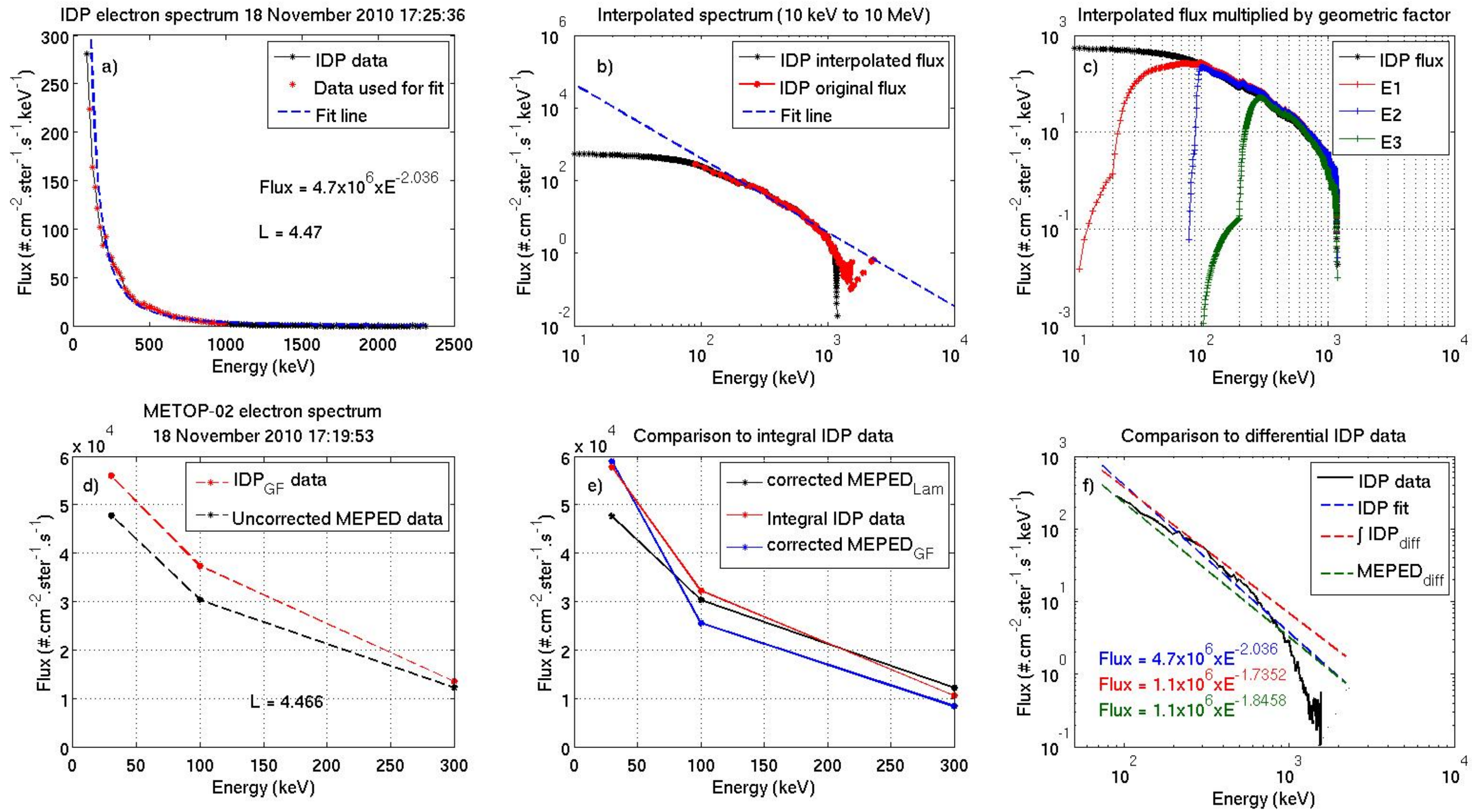

Figure 6: **a)** *The DEMETER spectrum for 18 November 2010 at 17:25:36UT, the black line shows the full data set while the red stars show the points used for the fitting (90 < E(keV) < 1000, blue line).* **b)** *The DEMETER data from panel* (a) *interpolated between 10 keV and 10 MeV in 1 keV intervals (black line) and shown in* log_{10} *space. The red points show the original spectrum and the fit shown in panel* (a) *is in blue.* **c)** *The interpolated IDP spectrum multiplied by the geometric factors in Yando et al. [2011] for each integral energy channel.* **d)** *The MEPED electron spectrum from 17:19:53UT on the same day, showing uncorrected integral electron flux (counts x100) in black and the simulation of these values by integrating the three curves shown in panel* (c) *and adding proton contamination.* **e)** *A comparison of the Lam proton corrected (black) and Yando proton and electron corrected (blue) POES data with the unaltered integral DEMETER fluxes (red).* **f)** *IDP differential flux repeated from panel* (b)*, the best fit is shown in blue with the differentiated Yando corrected POES data fit shown in green. As a test of the information lost by differentiated a 3 point fit to compare to a 40 point fit (red stars in panel* (a)*), the integral electron data from panel* (e) *is fitted, differentiated and shown in red. For a full description of each panel see Section 6.2.*

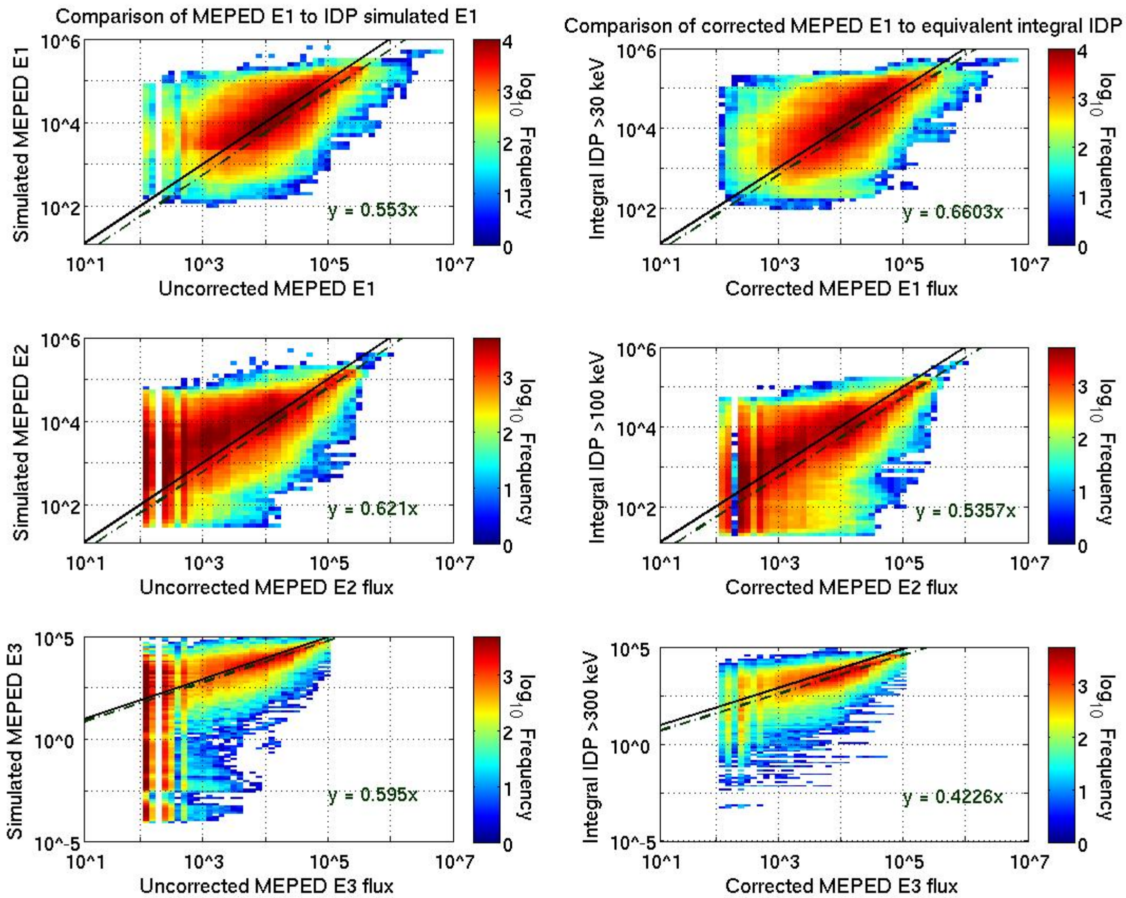

Figure 7: *Left: Binned scatter plot frequency graphs showing the comparison between the uncorrected MEPED data (counts multiplied by 100, on the x-axis) and the IDP data multiplied by the geometric factors in Yando et al. [2011] (described in Section 6.3). Right: Occurrence frequency plots of a similar style showing the comparison between the Lam corrected MEPED electron channels and the equivalent unmodified integral IDP data (described in Section 6.4). The top panels show E1 (>30 keV), the central panels show E2 (>100 keV) and the lower panels show E3 (>300 keV). The black solid line shows the* $y = x$ *relation and the green dash-dot line shows the* $y = mx$ *linear fit in each case.*

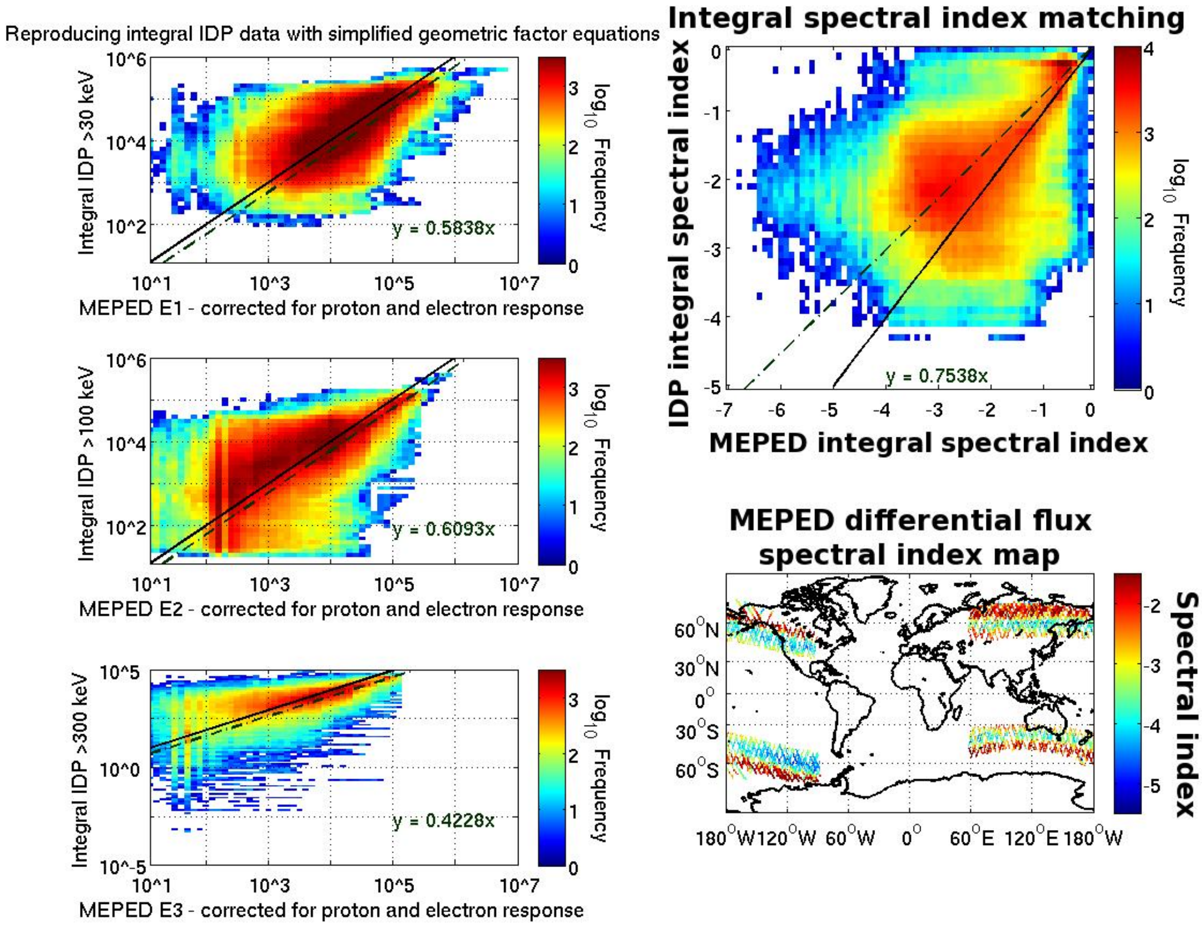

Figure 8: *Left: Occurrence frequency plots similar to Figure 7 which show the MEPED data corrected for electron detection efficiency and proton contamination (using Equations* (1)-(6)*) and compared to the unmodified integral IDP data. The* $y = x$ *relation is shown as the black solid line in the E1, E2 and E3 panels, while the best fit is shown by the green dash-dot line. Right top: The differential flux MEPED power-law spectral index compared to the differential IDP power-law spectral index, fit lines are included for* $y = x$ *(black) and the linear best fit with a zero y-intercept value* $y = 0.7538x$ *(green). Right lower: A global map showing the spatial distribution of the MEPED differential flux power-law spectral index (integral fit index - 1).*

Table 1: *Listing of the goodness-of-fit of a linear fit with gradient 1 for the three comparisons in Sections 6.3 to 6.5. The first column shows the* r^2 *value when the intercept value is 0, the second column shows the flux percentage change required to get the highest* r^2 *value, the third column lists this optimal fit coefficient and the final column shows the gradient when a linear* $y = mx$ *fit is applied to the data.*

	r^2 **of** $y = x$	**Optimal y reduction factor (a)**	**r**^{2} **of** $a \times y = x$	**Linear fit gradient**
Simulated MEPED values against raw MEPED data (Section 6.3)				
E1	0.289	44%	0.804	0.553
E2	0.547	39%	0.778	0.621
E3	0.208	43%	0.809	0.595
Corrected MEPED data against integral IDP (Section 6.4)				
E1	0.27	59%	0.705	0.66
E2	0.527	46%	0.823	0.536
E3	0.384	57%	0.884	0.423
GF corrected MEPED data against integral IDP (Section 6.5)				
E1	0.294	56%	0.675	0.584
E2	0.607	39%	0.775	0.609
E3	0.460	58%	0.874	0.423